Current detection using a Josephson parametric upconverter

Schmidt, Felix E.; Bothner, Daniel; Rodrigues, Ines C.; Gely, Mario F.; Jenkins, Mark D.; Steele, Gary A.

DOI
10.1103/PhysRevApplied.14.024069

Publication date
2020

Document Version
Final published version

Published in
Physical Review Applied

Current Detection Using a Josephson Parametric Upconverter

Felix E. Schmidt,* Daniel Bothner, Ines C. Rodrigues, Mario F. Gely, Mark D. Jenkins, and Gary A. Steele†

Kavli Institute of NanoScience, Delft University of Technology, Lorentzweg 1, Delft, 2628 CJ, The Netherlands

(Received 22 December 2019; revised 28 May 2020; accepted 8 July 2020; published 24 August 2020)

We present the design, measurement, and analysis of a current sensor based on a process of Josephson parametric upconversion in a superconducting microwave cavity. When a coplanar waveguide is terminated with a nanobridge-constriction Josephson junction, we observe modulation sidebands from the cavity that enable highly sensitive frequency-multiplexed output of small currents for applications such as readout of transition-edge sensor arrays. We derive an analytical model to reproduce the measurements over a wide range of bias current, detuning, and input power. When the frequency of the cavity is tuned by more than 100 MHz with a dc current, our device achieves a minimum current sensitivity of 8.9 pA/$\sqrt{\text{Hz}}$. Extrapolating the results of our analytical model, we predict an improved device based on our platform, capable of achieving a sensitivity down to 50 fA/$\sqrt{\text{Hz}}$, or even lower if one can take advantage of parametric amplification in the Josephson cavity. Taking advantage of the Josephson architecture, our approach can provide higher sensitivity than kinetic inductance designs, and potentially enables detection of currents ultimately limited by quantum noise.

DOI: 10.1103/PhysRevApplied.14.024069

I. INTRODUCTION

Ultralow-noise radiation detection has applications in astronomy, particle physics, and quantum information processing. In particular, transition-edge sensors (TESs) allow broadband radiation detection with exceptionally low noise-equivalent power [1] and photon-number resolution [2,3]. To read out the small changes in the current in TESs in response to radiation absorption, highly sensitive current amplifiers such as superconducting quantum interference devices (SQUIDs) can be used, with sensitivities as low as 4 fA/$\sqrt{\text{Hz}}$ [4]. However, with the increasing number of TESs to be read out simultaneously in multipixel detectors, SQUID amplifiers significantly increase the cost and complexity of the system, especially when frequency-domain multiplexing is employed to reduce the number of amplifiers necessary [5].

An example of the recently developed current detectors for use as a replacement for SQUIDs are kinetic inductance parametric upconverters (KPUPs), also referred to as microwave kinetic inductance nanowire galvanometers, which rely on the changing kinetic inductance L_k of a narrow superconducting wire embedded in a microwave circuit in response to a dc bias current, with state-of-the-art devices reaching current sensitivities $\mathcal{S}_I$ between 5 and 10 pA/$\sqrt{\text{Hz}}$ [6–8]. One could potentially achieve a higher response from such a cavity detector by replacing the nanowire kinetic inductance element with a Josephson junction (JJ), enabling detection of currents using a Josephson parametric upconverter (JPUP). This would also enable the incorporation of processes such as Josephson parametric amplification, which allows signals to be amplified with quantum-limited noise [9], directly in the readout cavity.

Typically, the integration of JJs in superconducting microwave circuits is technologically more demanding due to the additional fabrication steps needed to avoid aging effects and low coherence at microwave frequencies [10–13]. The intrinsically large Kerr nonlinearity of JJs [14] can additionally place an upper limit on the device power allowed for circuit operation, which calls for either large-critical-current JJs, with additional fabrication challenges [15], or appropriate circuit design to dilute the nonlinearity sufficiently to provide stable device operation.

Here, we provide an experimental realization of a JPUP based on a hybrid combination of a direct-current (dc)-accessible microwave cavity in a coplanar-waveguide (CPW) geometry [16,17]. The design uses a constriction JJ fabricated in the same step and layer as the microwave cavity, which simplifies the fabrication procedure and allows a high cavity drive power [18–21]. We show device operation by converting kilohertz current signals to the gigahertz range, and reproduce the data with an analytical model for a wide range of bias current, drive detuning, and drive power. Our device achieves performance comparable to KPUP technology, with the potential to provide enhanced current sensitivity with a more optimized design.

*f.e.schmidt@tudelft.nl
†g.a.steele@tudelft.nl

Ultimately, by using Josephson parametric amplification in the same cavity as that used for sensing, the JPUP could sense low-frequency currents with a sensitivity limited by quantum noise.

II. dc-BIAS MICROWAVE CIRCUIT

The device consists of a galvanically accessible microwave cavity, formed by a CPW that is shunted by an input capacitor C_s and shorted to ground at its far end by a JJ, as depicted in Figs. 1(a)–1(c). The JJ is formed by a narrow constriction in the superconducting base layer, which allows us to fabricate it in the same step as the microwave circuit. For details of the fabrication procedure, see Sec. SII in the Supplemental Material [22]. Because the shunt capacitor allows low-frequency signals to pass through but acts as a semitransparent mirror at microwave frequencies, our circuit allows simultaneous measurements in the dc and rf regimes.

In the dc regime, the CPW center conductor acts as a long lead to the JJ, which we use to perform a current-voltage measurement to characterize the JJ. Upon application of an increasing dc bias current, the JJ switches from the superconducting to the voltage state and back again at switching and retrapping currents $I_s \approx 8.5\ \mu$A and $I_r \approx 6.1\ \mu$A, respectively, as shown in Fig. 1(d). The observed hysteresis is most likely due to a combination of the capacitances of the CPW and the shunt capacitor and local heating in the junction area; see Refs. [23–26] and Sec. SIV in the Supplemental Material [22].

In the rf regime, the JJ acts as a nonlinear inductor, with its inductance L_J depending on the amount of bias current I_b flowing through it according to

$$L_J(I_b) = \frac{\Phi_0}{2\pi\sqrt{I_c^2 - I_b^2}}, \tag{1}$$

where I_c is the critical current and Φ_0 is the magnetic flux quantum. For zero bias current, the impedances of both the shunt capacitor and the JJ are small compared with the characteristic impedance of the CPW, i.e., $\omega L_J, 1/\omega C_s \ll Z_0$. The CPW can thus host a fundamental half-wavelength ($\lambda/2$) mode with current antinodes at both ends. When the reflected signal of the device is recorded using single-tone rf spectroscopy, the reflection signal shows a dip in the spectrum, as seen in Fig. 1(e). We fit the data using the

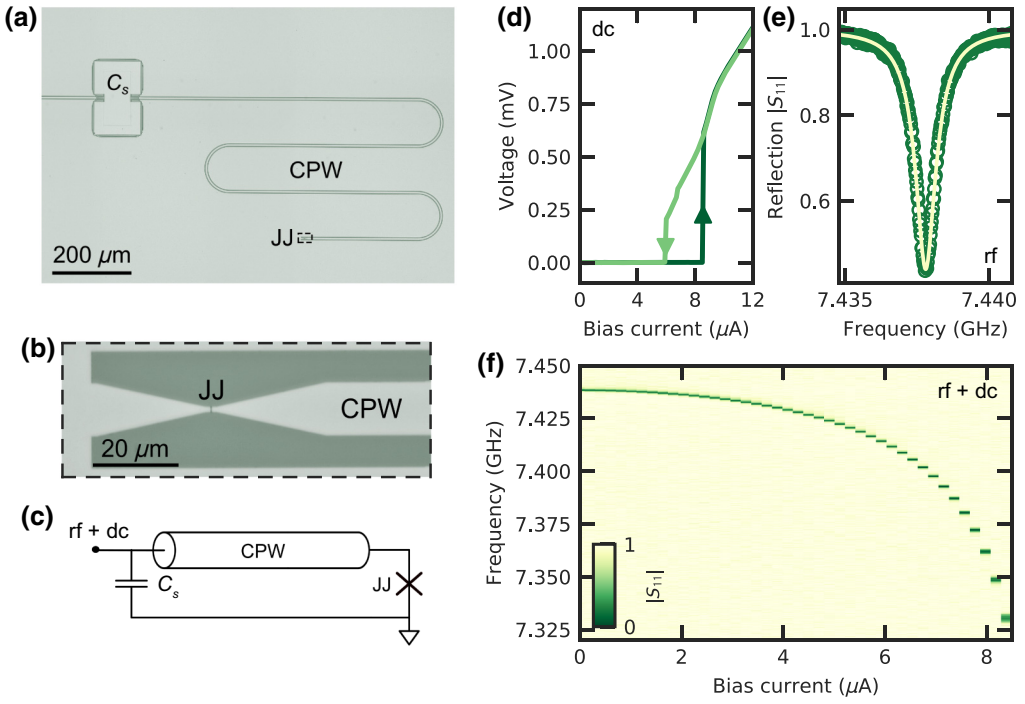

FIG. 1. Coplanar microwave Josephson circuit with direct-current bias. (a) Optical image of the measured device. This consists of a coplanar-waveguide transmission line shunted to ground via a parallel-plate capacitor C_s at the input, and a Josephson junction shorting the CPW center conductor to ground at the far end. (b) Optical close-up of the area around the JJ. (c) Schematic circuit layout. (d) Current-voltage characteristics of the JJ, measured by sweeping the bias current up and down (sweep direction indicated by arrows). (e) Normalized and background-corrected reflection $|S_{11}|$ of the device with zero bias current applied; see Sec. SIII A in the Supplemental Material [22]. Circles, data; line, fit. (f) Reflection coefficient $|S_{11}|$ as a function of bias current. Since the Josephson inductance increases with bias current, the resonance frequency of the circuit shifts towards lower values.

reflection coefficient of our circuit,

$$S_{11} = \frac{\kappa_e - \kappa_i - 2i\Delta}{\kappa_e + \kappa_i + 2i\Delta}, \tag{2}$$

where $\Delta = \omega - \omega_0$ is the detuning between the drive at ω and the resonance frequency ω_0, and the external and internal loss rates are κ_e and κ_i, respectively [16]. At zero bias current, we find a resonance frequency of $\omega_0 = 2\pi \times 7.438$ GHz and linewidths of $\kappa_e = 2\pi \times 624$ kHz and $\kappa_i = 2\pi \times 261$ kHz. Here, the external loss rate κ_e describes how much signal leaks to the feed line, while κ_i captures intracavity losses such as those due to dielectrics or radiation; see Sec. SIII A in the Supplemental Material.

As we dc-bias the circuit, L_J increases, effectively shifting the voltage antinode closer to the JJ. This results in a continuously decreasing resonance frequency, which can be tuned over approximately 108 MHz; see Fig. 1(f). We can approximate the bias-current dependence of the cavity resonance frequency with a model describing a $\lambda/2$ CPW resonator terminated by a JJ via

$$\omega_0(I_b) = \omega_{\lambda/2}\frac{L_r + L_J(I_b, I_c)}{L_r + 2L_J(I_b, I_c)}, \tag{3}$$

where $\omega_{\lambda/2}$ is the resonance frequency of the CPW directly shorted to ground, and L_r is the total inductance of the bare resonator (see Sec. SIII C in the Supplemental Material [22] and in Ref. [27]). We use this model to fit the measured resonance frequencies in Fig. 2(a), from which we extract $\omega_{\lambda/2} = 2\pi \times 7.515$ GHz, $L_r = 3.401$ nH, and $I_c = 9.157$ μA. The resonator inductance agrees with the value expected from our circuit design. The critical current inferred from the microwave measurement is approximately 8% larger than the dc switching current. We suspect that current noise in the dc line leads to premature switching of the JJ in the I-V measurements, resulting in $I_s < I_c$, as discussed in Sec. SV in the Supplemental Material [22] and in Ref. [28]. On the other hand, the rf measurement is sensitive to the Josephson inductance, from which we can infer the critical current in a less perturbative way. We note that current-biasing a superconducting wire also changes its kinetic inductance L_k [29,30]. However, while our device possesses a noticeable kinetic inductance fraction [31], the changes in L_k within the range of bias currents applied are negligible compared with L_J, and we thus attribute the resonance-frequency shift completely to the latter; see Sec. SIII B in the Supplemental Material [22].

We note that upon increasing the dc bias current I_b, we observe an increase in the internal loss rate κ_i of our device. We find that the dependence $\kappa_i(I_b)$ can be approximated by a constant term and an exponential growth, which we ascribe to a combination of low-frequency electrical interference in the dc bias current and phase diffusion across the JJ; see Sec. SV in the Supplemental Material [22].

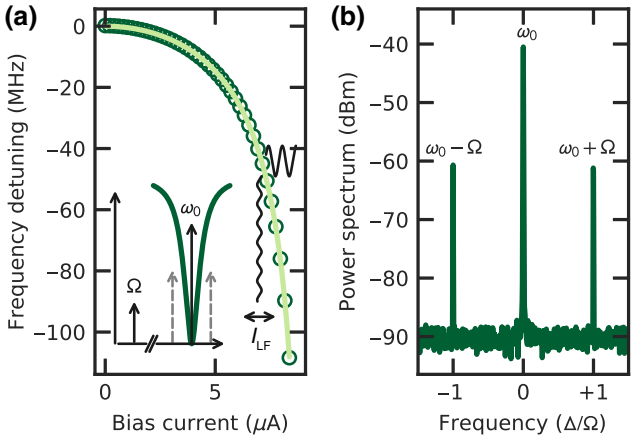

FIG. 2. Current detection by frequency upconversion. (a) Cavity resonance frequency for increasing dc bias current, showing a total frequency shift of 108 MHz. Circles, measured data; line, fit to resonance frequency using Eq. (3). Inset: sketch of measurement scheme in the frequency domain. When the cavity is driven on resonance at $\omega = \omega_0$ and simultaneously modulated with a low-frequency current $\delta I = I_{\rm LF}\cos\Omega t$, the cavity generates sidebands of the drive tone at $\omega_0 \pm \Omega$ (dashed gray arrows). (b) Power spectrum of the reflected field at $I_b = 2.5$ μA, containing the input pump signal at ω_0 and the first-order sidebands due to mixing at $\omega_0 \pm \Omega$. The noise floor sets a lower limit on the smallest detectable sideband amplitude. The sideband amplitude allows us to directly calibrate the noise floor and thus the sensitivity from the signal-to-noise ratio (SNR), here approximately 30 dB.

III. CURRENT DETECTION BY FREQUENCY UPCONVERSION

Figure 2(a) illustrates the principle of current detection using the dc-biased Josephson cavity. To detect small modulation currents, we drive the cavity on resonance at $\omega_0(I_b)$ and simultaneously modulate the bias point I_b with a low-frequency signal $\delta I = I_{\rm LF}\cos\Omega t$, so that the total current is given by $I = I_b + I_{\rm LF}\cos\Omega t$. The responsivity of the resonance frequency to the bias current,

$$G_1 = \frac{\partial\omega_0}{\partial I_b}, \tag{4}$$

exceeds $2\pi \times 100$ MHz μA^{-1} for $I_b \gtrsim 8$ μA. As a consequence, once the resonance frequency is modulated by $I_{\rm LF}$, phase modulation leads to the generation of sidebands in the microwave drive-tone reflection with $\omega = \omega_d \pm n\Omega$, where $n \in \mathbb{Z}$. The reflected cavity field thus exhibits the drive tone together with the sidebands, as depicted in Fig. 2(b).

The general equation of motion for the amplitude field α of a harmonic high-Q oscillator with a small nonlinearity β, written in the frame rotating with the drive, is

given by

$$\dot{\alpha} = \left[-i\left(\Delta + \beta|\alpha|^2\right) - \frac{\kappa}{2}\right]\alpha + \sqrt{\kappa_e}S_{\text{in}}, \tag{5}$$

where S_{in} is the amplitude of the drive field in units of $\sqrt{\text{photons/Hz}}$ at ω [32]. We consider the case in which the cavity resonance frequency is a function of an additional current given by $I = I_b + \delta I = I_b + I_{\text{LF}}\cos\Omega t$, such that

$$\omega_0 = \omega_0(I_b) + \sum_{m=1}^{n}\frac{\partial^m\omega_0}{\partial I^m}\,\delta I^m = \omega_I + \sum_{m=1}^{n} G_m\,\delta I^m. \tag{6}$$

The resulting field amplitude of the first-order sidebands appearing at $\omega_0 \pm 1\Omega$ is

$$|S_{\pm1}|^2 = \frac{\kappa_e\alpha_0^2 G_1^2 I_{\text{LF}}^2}{\kappa^2 + 4(\Delta \pm \Omega)^2}. \tag{7}$$

In our experiment, we choose $\Omega = 2\pi \times 1$ kHz and $I_{\text{LF}} = 10$ nA. In this case, $\Omega \ll \kappa$, and the red (S_-) and blue (S_+) sidebands have approximately equal amplitudes; see Sec. SVII in the Supplemental Material [22]. Note that even higher-order contributions from the current still contribute to the $\pm1\Omega$ sideband, but those contributions can be neglected for relatively weak modulation.

To explore the parameter space of our device, we perform a series of current-mixing measurements for different values of the bias current I_b, the drive detuning Δ, and the drive amplitude S_{in}, for all of which we observe excellent agreement between experiment and theory. As can be seen in Fig. 3(a), for the case of varying bias current, and as expected from Eqs. (3) and (7), the first-order sideband vanishes for zero bias current. As we increase the dc bias current, the increasing Josephson inductance leads to an increased responsivity $\partial\omega_0/\partial I_b$, which in turn results in a growing sideband amplitude. Assuming all other parameters remain constant, the sideband amplitude should keep growing until the bias current reaches the critical current of the JJ, at which point the junction switches to the normal state, effectively destroying the device response. However, at $I_b \approx 0.75\,I_c$, the sideband amplitude already exhibits a maximum value and begins to decrease subsequently. The origin of this phenomenon lies in the growth of κ_i with increasing I_b, as described earlier, which limits the maximum achievable sideband amplitude; see Sec. SIV B and Sec. SV in the Supplemental Material [22].

Operating the device at constant bias current and drive power P_{in} but sweeping the drive tone with respect to the cavity resonance similarly reduces the sideband amplitude, which is reflected in both the theoretical model and our measurements; see Fig. 3(b). We attribute the deviations of the model from the data to an effectively increased cavity linewidth resulting from a noise-induced fluctuating cavity frequency.

Finally, when we set the detuning back to zero and sweep the drive power, we initially observe a linear increase in the sideband amplitude; see Fig. 3(c). This is in good agreement with the dependence of the intracavity field on the pump power for a linear cavity. However, due to the nonlinearity of the JJ and the resulting Kerr anharmonicity of the circuit, our device enters the Duffing regime for large input power, resulting in an observable reduction of the sideband amplitude: the anharmonicity results in a downshifted resonance frequency given by $\omega_0' = \omega_0 - |\alpha_0|^2\beta$. In the measurement depicted

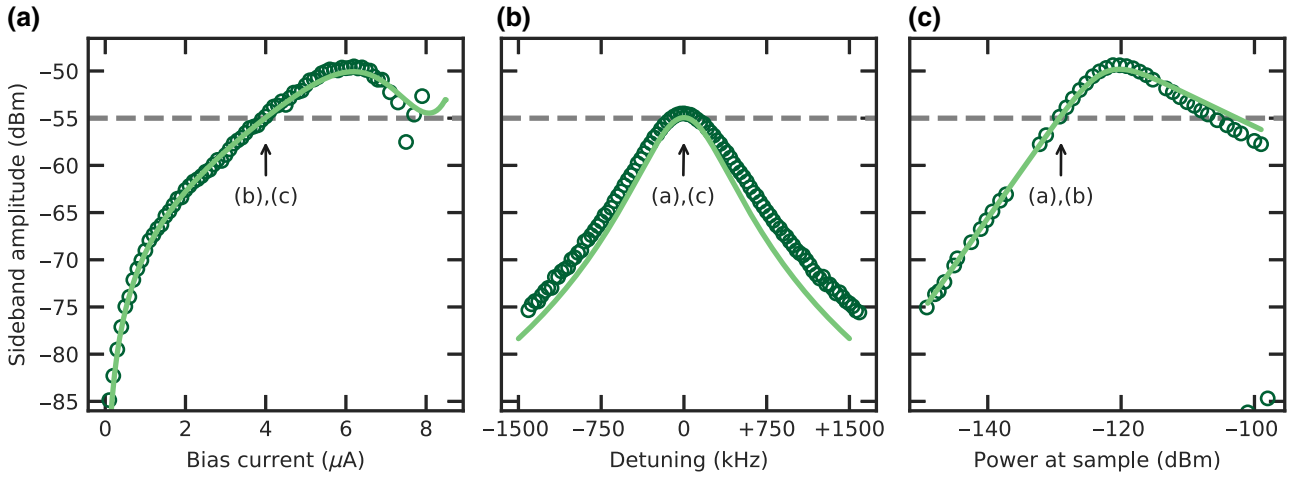

FIG. 3. Exploring the parameter space for the first-order sideband amplitude. (a) Sideband height for changing bias-current setpoint at fixed input power and zero detuning. (b) Sideband height for changing drive detuning at fixed input power and bias current. (c) Sideband height for changing input power at fixed bias current and detuning. Circles, measured data; solid lines, amplitude calculated via input-output theory; dashed gray lines, calculated sideband amplitude at $I_b = 4\ \mu$A, $\Delta = 0$, and $P_{\text{in}} = -129$ dBm. The arrows indicate the setpoints for the other figure parts.

in Fig. 3(c), the only varying parameter is the pump power, which means that in the Duffing regime the drive acquires an increase in detuning with increased power, resulting in a decreased sideband amplitude, as we saw earlier.

IV. CURRENT SENSITIVITY

Having established the validity of our theoretical framework, we calculate the current sensitivity $\mathcal{S}_I$ of our device. This quantity captures the minimum current that the device is able to discriminate from the noise floor. We obtain this quantity by extracting the SNR of the first sideband amplitude: since we know the amplitude of our ingoing LF current signal, we can convert the sideband amplitude and noise floor to currents as described in Sec. SIX in the Supplemental Material [22]. We obtain

$$\mathcal{S}_I = \frac{I_{\mathrm{LF}}}{\sqrt{B_e \times 10^{(S-N)/10}}}, \tag{8}$$

where B_e is the equivalent noise bandwidth of the spectrum analyzer [33], and S and N are the amplitudes of the sideband and the noise floor, respectively, in dBm.

A. Measured device

We analyze $\mathcal{S}_I$ for a large range of the bias current and drive power. The device sensitivities extracted via Eq. (8) are plotted in Figs. 4(a) and 4(b) for the measured and modeled data, respectively, showing good qualitative agreement. Line sections through the two-dimensional measured and simulated data at the best measured value of $\mathcal{S}_I$ show good quantitative agreement between the theoretical model and the measurements; see Figs. 4(c) and 4(d).

For a fixed bias current, the current sensitivity drops exponentially as a function of input power, reaching a minimum value of $\mathcal{S}_I = 8.9\ \mathrm{pA}/\sqrt{\mathrm{Hz}}$ at $I_b = 7.3\ \mu\mathrm{A}$ and $P_{\mathrm{in}} = -113$ dBm. Similarly, as a function of bias current at fixed input power, the current sensitivity drops rapidly by more than 2 orders of magnitude. Our theoretical calculations deviate from the measured data for very large input power and bias current, for which the model predicts sensitivity values larger than observed. This deviation might be due to minor differences in the experimental and theoretical detunings: if the pump tone ω_0 is slightly below the value of ω_0' in the limit of $n_{\mathrm{ph}} \to 0$, the pump will initially be slightly red-detuned ($\Delta < 0$) and move to blue-detuned ($\Delta > 0$) as the resonance shifts downward due to the Kerr nonlinearity, instead of starting on resonance and becoming only blue-detuned as we increase P_{in}. Depending on the pump power at which $\Delta = 0$, the theoretical curve will underestimate the sideband amplitude for $\Delta > 0$, resulting in values of $\mathcal{S}_I$ that are too large, as in Fig. 4(c) for $P_{\mathrm{in}} \geq -120$ dBm.

As detailed in Sec. SVIII B in the Supplemental Material [22], the model follows the measured data more closely for high pump power, assuming an initially red-detuned drive. This deviation is especially large for high bias currents because the anharmonicity grows with I_b. Thus, the cavity resonance shifts more strongly with pump power,

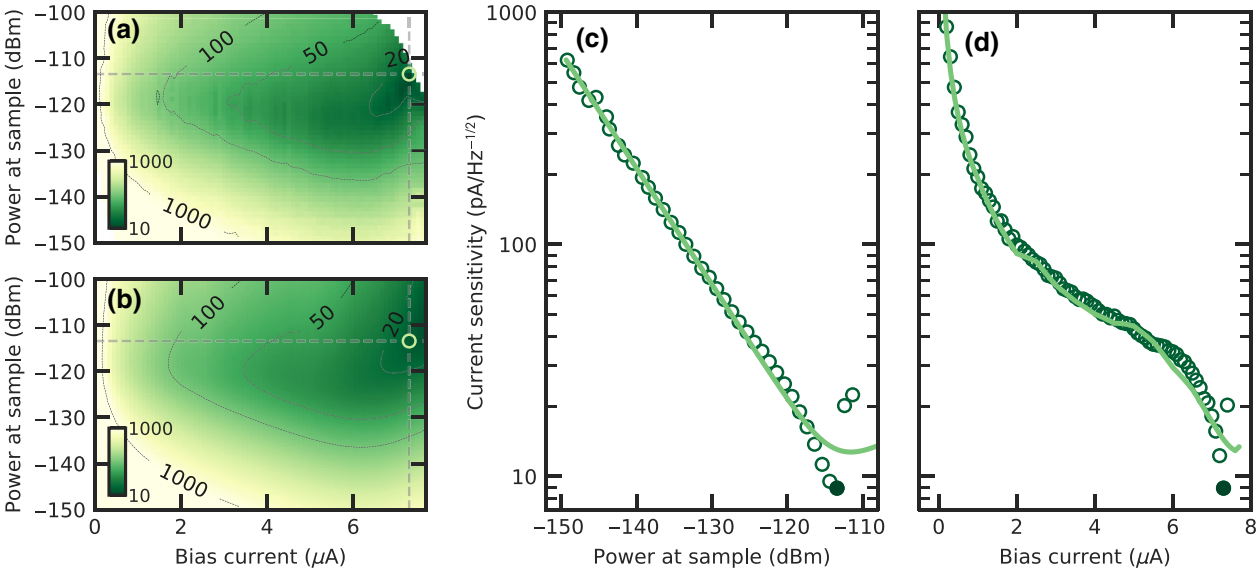

FIG. 4. Finding the best device sensitivity. Current sensitivity in $\mathrm{pA}/\sqrt{\mathrm{Hz}}$ versus bias current and input power, as measured (a) and as calculated (b). The dashed gray lines correspond to the line sections in (c),(d), and the circles mark the point of minimum measured sensitivity. The color scale is logarithmic from 10 to 1000, and the black lines mark contour lines of sensitivity values as labeled. (c) Sensitivity at 7.3 μA versus pump power [vertical lines in (a),(b)]. We attribute the discrepancies at high P_{in} to differences in Δ between the measurement and theory. (d) Sensitivity at $P_{\mathrm{in}} = -113$ dBm versus bias current [horizontal lines in (a),(b)]. Circles, measured data; lines, model; filled circles, minimum measured sensitivity.

and the drive is more likely to have a smaller detuning than expected for high P_{in}.

B. Limitations of present device and setup

Optimum sensitivity would be achieved for zero pump detuning, maximum pump power, and biasing the device close to I_c; see Figs. 4(a) and 4(b). In our experiment, we are unable to operate the device in a stable regime for bias currents greater than $0.9I_c$, after which the JJ occasionally switches to the normal state, destroying the rf resonance. We attribute this to a significant ac current induced by the microwave drive, on the order of 1 μA; see Sec. SVI in the Supplemental Material [22]. Together with the dc bias, the total current at the JJ reaches close to I_c, thus constraining the available parameter space.

Additionally, we observe an exponential increase in the internal loss rate at large bias current. This effect is presumably due to random phase diffusion across the junction and electrical interference in our setup; see Sec. SV in the Supplemental Material [22]. Most notably, at elevated bias currents spurious sidebands at integer multiples of 50 Hz appear in the measured spectra, which are due to insufficient isolation between the dc and rf electronics. Using the same approach as for the intended signal, we can quantify the current noise due to mains power as 170 pA $\approx I_{\text{LF}}/60$. Improving the setup should allow us to move to even higher bias currents, gaining in $\mathcal{S}_I$. In addition, the resonance-frequency shift due to anharmonicity places an upper bound on the maximum input power.

In an optimized measurement, shifting the pump frequency with the pump power in order to remain closer to resonance should allow us to gain more than 10 dB, reaching a minimum of 2.7 pA/$\sqrt{\text{Hz}}$; see Sec. SVIIIA in the Supplemental Material [22].

C. Modeled optimized device

In order to improve $\mathcal{S}_I$, we propose a slightly changed circuit layout that follows naturally from the measured device and is immediately implementable: instead of a transmission line shorted to ground by a single JJ, we propose to incorporate the Josephson inductance into the transmission line itself, by means of a diluted JJ metamaterial [34]. The optimized design would then be a transmission line directly shorted to ground, with the CPW center conductor made up of a series of identical unit cells, each composed of a combination of linear and Josephson inductances (L_0, L_J) and a capacitance to ground (C_0), as depicted in Fig. 5(a). Following the approach to circuit quantization presented in Ref. [35] and methods from Refs. [36–38], we derive the resonance frequency of this CPW as

$$\omega_0(I_b) = \frac{\pi}{N\sqrt{C_0[L_J(I_b) + L_0]}}, \tag{9}$$

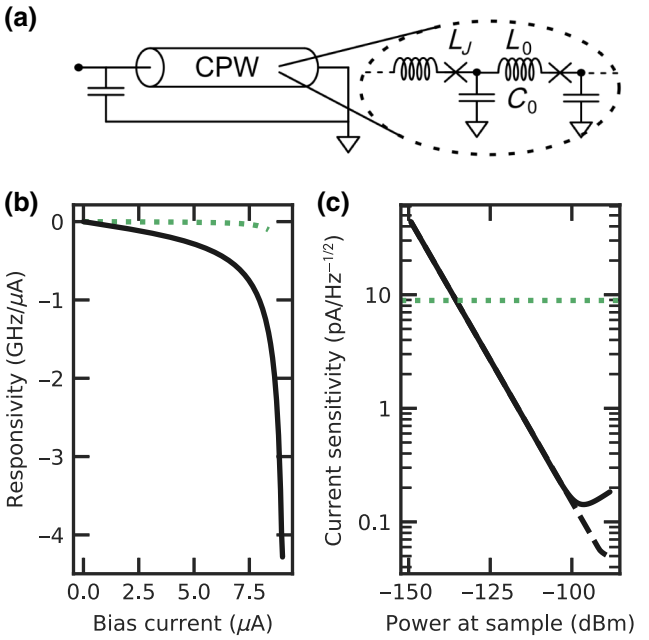

FIG. 5. Estimated sensitivity for optimized device design. (a) Instead of a linear CPW shorted to ground by a nonlinear Josephson junction, the optimized device is a diluted JJ metamaterial with a CPW center conductor based on a Josephson-junction array, directly shorted to ground. (b) Frequency responsivity G_1 for the optimized (solid line) and current (dotted line) device. Because of the dominating Josephson inductance, the optimized device can be tuned further with bias current. (c) Predicted $\mathcal{S}_I$ for the optimized device. The dotted line indicates the minimum experimentally achieved sensitivity of 8.9 pA/$\sqrt{\text{Hz}}$ with the present design. For the JJ-array CPW, we predict a sensitivity as low as 170 fA/$\sqrt{\text{Hz}}$ (solid line). The sensitivity curves upwards at high pump power due to the nonlinearity in the circuit. If the pump frequency is chosen to be continuously close to resonance for high drive power, the predicted sensitivity drops to 50 fA/$\sqrt{\text{Hz}}$ (dashed line). Parametric amplification could reduce the sensitivity 1 order of magnitude further by reducing the contribution of the noise of the cryogenic HEMT amplifier to the readout noise of the cavity.

in the limit of large N, as detailed in Sec. SXI in the Supplemental Material [22]. To maximize the responsivity G_1 of the device via maximizing the participation ratio $\eta_J = L_J/(L_0 + L_J)$ per unit cell, we propose a CPW with center-conductor and gap sizes one tenth of those of the current design and a reasonably short unit-cell length of 1 μm. This would result in $L_0 = 842$ fH, $L_J = 35.9$ pH, and $C_0 = 169$ aF per unit cell; see Ref. [39] and Sec. SXI in the Supplemental Material [22]. For an initial resonance frequency of $\omega_0 = 2\pi \times 7.5$ GHz, the device would require approximately 845 unit cells, resulting in a total device length of 845 μm, much more compact than our present layout. Such an optimized device offers a significantly larger $G_1 \approx 4$ GHz μA^{-1} with a relative frequency shift $\delta\omega_0/\omega_0 \approx 50\%$. Assuming the same internal losses

as for our measured device and additionally assuming an increased external coupling, which could be achieved, e.g., by reducing the shunt capacitor to half of its current area, this device would be able to achieve a sensitivity as low as 0.17 pA/$\sqrt{\text{Hz}}$, a factor of 54 improvement on our design presented above, as shown in Fig. 5(b).

We note that in an ideal experiment, the drive frequency should be tuned with increasing drive power in order to account for the Kerr shift of the resonance to lower frequencies, thus minimizing Δ and maximizing α_0. Implementing this measurement scheme would allow us to achieve a sensitivity down to 50 fA/$\sqrt{\text{Hz}}$. Since this estimate does not take parametric amplification into account, we expect it to be an upper bound on the experimentally achievable $\mathcal{S}_I$: utilizing quantum-limited parametric amplification built into the device would allow us to gain approximately 20 dB [9,27,34], providing noise levels down to 5 fA/$\sqrt{\text{Hz}}$.

V. CONCLUSION

We present a Josephson parametric upconverter and demonstrate current sensitivities down to 8.9 pA/$\sqrt{\text{Hz}}$, which makes our device compatible with TES readout, and derive an analytical model that accurately reproduces the measured data and is immediately applicable to other device architectures. We estimate that future devices using increased Josephson participation ratios, and using the intrinsic Kerr nonlinearity for four-wave parametric amplification built into the detection cavity, should allow an improved $\mathcal{S}_I \sim 5$ fA/$\sqrt{\text{Hz}}$, orders of magnitude better than state-of-the-art KPUPs and limited by the fundamental quantum noise of the cavity.

DATA AVAILABILITY

All raw and processed data, as well as supporting code for measurement libraries, data processing, and figure generation, are available on Zenodo [40].

ACKNOWLEDGMENTS

This project received funding from the European Union Horizon 2020 research and innovation program under Grants No. 681476–QOMD, No. 732894–HOT, and No. 785219–GrapheneCore2.

APPENDIX A: INPUT-OUTPUT FORMALISM

Starting from Eq. (5), with the steady-state solution α_0, the reflection coefficient is given by

$$S_{11} = -1 - \sqrt{\kappa_e}\frac{\alpha_0}{S_{\text{in}}} = -1 + \frac{2\kappa_e}{\kappa + 2i\Delta}, \tag{A1}$$

where the second equality holds in the limit $\beta \to 0$ and can be recognized as the usual expression for reflection in circuit theory.

We now consider the case in which the cavity resonance frequency is a function of an additional current given by $I = I_b + \delta I$. With the resonance frequency given by Eq. (6), the new equation of motion reads

$$\dot{\alpha} = \left[-i\left(\Delta - \sum_{m=1}^{n} G_m\,\delta I^m\right) - \frac{\kappa}{2}\right]\alpha - i\beta|\alpha|^2\alpha + \sqrt{\kappa_e}S_{\text{in}}. \tag{A2}$$

With the ansatz for the intracavity field $\alpha(t) = \alpha_0 + \delta\alpha(t)$ and assuming $|\alpha|^2 \approx \alpha_0^2$, we get

$$\delta\dot{\alpha} = \left[-i\left(\Delta - \sum_{m=1}^{n} G_m\,\delta I^m\right) - \frac{\kappa}{2}\right]\delta\alpha + i\alpha_0\sum_{m=1}^{n} G_m\,\delta I^m. \tag{A3}$$

Let the modulation of the current be of the form

$$\delta I = I_{\text{LF}}\cos\Omega t = I_- e^{-i\Omega t} + I_+ e^{+i\Omega t}, \tag{A4}$$

where $I_- = I_+ = I_{\text{LF}}/2$. Our ansatz for $\delta\alpha$ is consequently

$$\delta\alpha = \sum_{m=1}^{n} a_{-m}e^{-mi\Omega t} + a_{+m}e^{+mi\Omega t}. \tag{A5}$$

Inserting Eqs. (A4) and (A5) into Eq. (A3), we can group the terms by their frequency components and equalize each component individually in order to solve for the sideband coefficients $a_{\pm m}$. Each sideband output field can then be calculated via

$$S_{\pm m} = \sqrt{\kappa_e}a_{\pm m}. \tag{A6}$$

We arrive at a compact result for the first-order sidebands appearing at $\omega_0 \pm 1\Omega$:

$$S_{\pm 1} = \frac{\sqrt{\kappa_e}\alpha_0 G_1 I_{\text{LF}}}{-i\kappa + 2(\Delta \pm \Omega)}. \tag{A7}$$

We calculate all coefficients $a_{\pm m}$ up to $m = 3$ using *Mathematica* v11.3.0.0 in the notebook `input-output formalism.nb`, which we subsequently convert to PYTHON3 code using the notebook `Export to Python.nb` located on Zenodo [40].

APPENDIX B: CALCULATING THE STEADY-STATE SOLUTION

We can calculate α_0 by solving Eq. (5) for a large pump signal and treating the probe as a perturbation. Thus, let us assume that the solution has the form $\alpha(t) = \alpha_0 \exp[i\omega_p t]$

and that the input signal $S_{\rm in}(t) = S_p(t) = S_{p0}\exp[i(\omega_p t + \phi)]$ is the pump signal. Since we are interested only in the steady-state solution, let $S_{p0}, \alpha_0 \in \mathbb{R}$. Inserting this into Eq. (5), we get

$$\left(i\Delta + \frac{\kappa}{2}\right)\alpha_0 + i\beta\alpha_0^3 = \sqrt{\kappa_e}S_{p0}e^{i\phi}. \tag{B1}$$

Multiplying this equation by its complex conjugate returns

$$\beta^2\alpha_0^6 + 2\Delta\beta\alpha_0^4 + \left(\Delta^2 + \frac{\kappa^2}{4}\right)\alpha_0^2 - \kappa_e S_{p0}^2 = 0. \tag{B2}$$

While this third-order polynomial in α_0^2 has multiple complex solutions, the ones relevant to our case are real only. In the high-power regime, our resonator exhibits bifurcation and Duffing behavior, meaning that there are three real-valued solutions for α_0^2, the largest, median, and smallest ones corresponding to the high-, middle-, and low-amplitude branches, respectively. For a given input field S_{p0} and detuning Δ, the (up to three) solutions of this equation can be found either numerically or analytically. However, for the parameters used in our experiment, the solutions for α_0^2 are identical because our drive remains outside the bifurcation regime. We can then use the corrected intracavity field to obtain the sideband amplitudes by replacing the value of α_0 for the linear oscillator in Eq. (A7).

Furthermore, taking the resonance frequency as the point where $\partial\alpha_0/\partial\omega = 0$, we can compute the frequency shift that the cavity experiences as a result of the driving power by differentiating Eq. (B2) with respect to ω, obtaining

$$\omega_0' = \omega_0 - |\alpha_0|^2\beta. \tag{B3}$$

APPENDIX C: HIGHER-ORDER TERMS

At second order in δI, the prefactors are already too complicated to write down in a short form, which is why we refer to the full analytical solutions in the *Mathematica* notebook `input-output formalism.nb` located on Zenodo [40]. We note that higher-order corrections arising for terms in δI^m have only negligible effects on the lower-order forms. For the analysis in the main text, we therefore make use of the closed form only for the first-order terms; for the second-order peaks in Figs. 6(b)–6(d), only the second-order terms are used.

We observe higher-order sidebands over a wide range of operating points, with an example spectrum exhibiting both first- and second-order peaks plotted in Fig. 6(a). Similarly to Fig. 3(a), the second-order sideband increases with the dc bias current up to $I_b \approx 0.75 I_c$, where the amplitude is limited by the increasing internal loss rate; see Fig. 6(b). As depicted in Fig. 6(c), a finite drive detuning strongly suppresses the sideband amplitude similarly to the case for the first-order peaks. The power dependence [see Fig. 6(c)] also closely resembles the shape of the first-order sideband, with maximum amplitude for high drive power and a subsequent decrease due to increasing drive detuning as a consequence of the downshift in resonance frequency due to the Kerr nonlinearity.

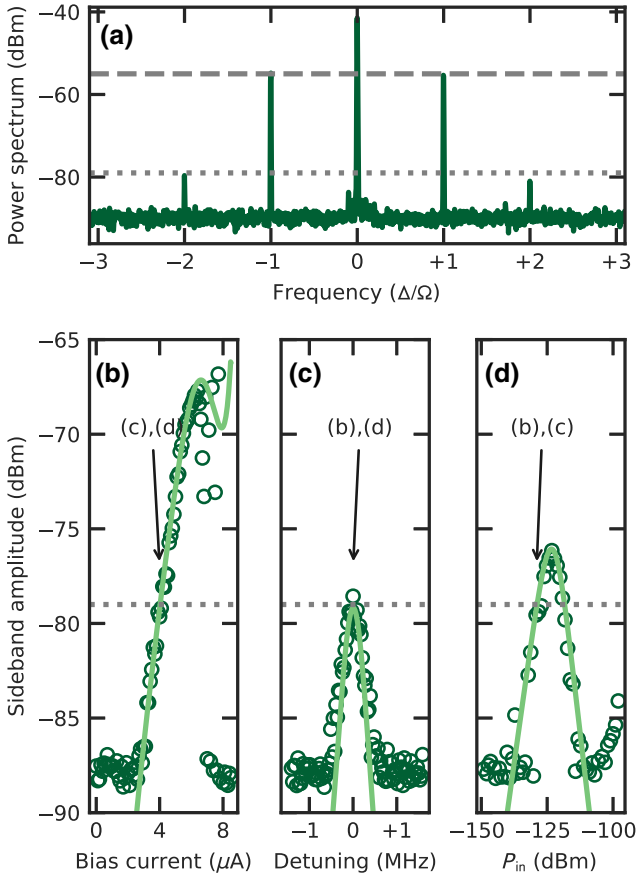

FIG. 6. Exploring the parameter space for the second-order sideband amplitude. (a) Power spectrum at the output at $I_0 = 4\ \mu$A, $\Delta = 0$, and $P_{\rm in} = -129$ dBm, containing the input pump signal at ω_0 and the first- and second-order sidebands due to mixing at $\omega_0 \pm \Omega$ and $\omega_0 \pm 2\Omega$. The dotted gray line corresponds to the dotted gray lines in parts (b)–(d), and the dashed gray line corresponds to the dashed gray lines in Fig. 3. (b) Sideband height for changing bias-current setpoint at fixed input power and zero detuning for the varying bias current. (c) Sideband height for changing drive detuning at fixed input power and bias current. (d) Sideband height for changing input power at fixed bias current and detuning. Circles, measured data; solid lines, amplitude calculated via input-output theory; dotted gray lines, calculated sideband amplitude at $I_0 = 4\ \mu$A, $\Delta = 0$, and $P_{\rm in} = -129$ dBm. The arrows indicate the setpoints for the other figure parts.

[1] D. J. Goldie, A. V. Velichko, D. M. Glowacka, and S. Withington, Ultra-low-noise MoCu transition edge sensors for space applications, J. Appl. Phys. **109**, 084507 (2011).

[2] B. Cabrera, R. M. Clarke, P. Colling, A. J. Miller, S. Nam, and R. W. Romani, Detection of single infrared, optical, and ultraviolet photons using superconducting transition edge sensors, Appl. Phys. Lett. **73**, 735 (1998).

[3] A. J. Miller, S. W. Nam, J. M. Martinis, and A. V. Sergienko, Demonstration of a low-noise near-infrared photon counter with multiphoton discrimination, Appl. Phys. Lett. **83**, 791 (2003).

[4] F. Gay, F. Piquemal, and G. Genevès, Ultralow noise current amplifier based on a cryogenic current comparator, Rev. Sci. Instrum. **71**, 4592 (2000).

[5] S. W. Henderson *et al.*, in *SPIE Astronomical Telescopes + Instrumentation*, edited by W. S. Holland and J. Zmuidzinas (Edinburgh, United Kingdom, SPIE, 2016) p. 99141G.

[6] A. Kher, P. K. Day, B. H. Eom, J. Zmuidzinas, and H. G. Leduc, Kinetic inductance parametric up-converter, J. Low Temp. Phys. **184**, 480 (2016).

[7] S. Doerner, A. Kuzmin, K. Graf, I. Charaev, S. Wuensch, and M. Siegel, Compact microwave kinetic inductance nanowire galvanometer for cryogenic detectors at 4.2 K, J. Phys. Commun. **2**, 025016 (2018).

[8] A. Kuzmin, S. Doerner, S. Singer, I. Charaev, K. Ilin, S. Wuensch, and M. Siegel, Terahertz transition-edge sensor with kinetic-inductance amplifier at 4.2 K, IEEE Trans. Terahertz. Sci. Technol. **8**, 622 (2018).

[9] J. Stehlik, Y.-Y. Liu, C. M. Quintana, C. Eichler, T. R. Hartke, and J. R. Petta, Fast Charge Sensing of a Cavity-Coupled Double Quantum Dot Using a Josephson Parametric Amplifier, Phys. Rev. Appl. **4**, 014018 (2015).

[10] A. B. Pavolotsky, D. Dochev, and V. Belitsky, Aging- and annealing-induced variations in Nb/Al–AlOx/Nb tunnel junction properties, J. Appl. Phys. **109**, 024502 (2011).

[11] U. S. Goteti, M. Denton, K. Krause, A. Stephen, J. A. Sellers, S. Sullivan, M. C. Hamilton, A. Wynn, and S. K. Tolpygo, Reliability studies of Nb/AlOx/Al/Nb Josephson junctions through accelerated-life electrical stress testing, IEEE Trans. Appl. Supercond. **29**, 1 (2019).

[12] D. Gunnarsson, J.-M. Pirkkalainen, J. Li, G. S. Paraoanu, P. Hakonen, M. Sillanpää, and M. Prunnila, Dielectric losses in multi-layer Josephson junction qubits, Supercond. Sci. Technol. **26**, 085010 (2013).

[13] S. Yanai and G. A. Steele, Observation of enhanced coherence in Josephson SQUID cavities using a hybrid fabrication approach, arXiv:1911.07119 (2019).

[14] A. Wallraff, D. I. Schuster, A. Blais, L. Frunzio, R.-S. Huang, J. Majer, S. Kumar, S. M. Girvin, and R. J. Schoelkopf, Strong coupling of a single photon to a superconducting qubit using circuit quantum electrodynamics, Nature **431**, 162 (2004).

[15] F. Lecocq, I. M. Pop, Z. Peng, I. Matei, T. Crozes, T. Fournier, C. Naud, W. Guichard, and O. Buisson, Junction fabrication by shadow evaporation without a suspended bridge, Nanotechnology **22**, 315302 (2011).

[16] S. J. Bosman, V. Singh, A. Bruno, and G. A. Steele, Broadband architecture for galvanically accessible superconducting microwave resonators, Appl. Phys. Lett. **107**, 192602 (2015).

[17] F. E. Schmidt, M. D. Jenkins, K. Watanabe, T. Taniguchi, and G. A. Steele, A ballistic graphene superconducting microwave circuit, Nat. Commun. **9**, 4069 (2018).

[18] R. Vijay, J. D. Sau, M. L. Cohen, and I. Siddiqi, Optimizing Anharmonicity in Nanoscale Weak Link Josephson Junction Oscillators, Phys. Rev. Lett. **103**, 087003 (2009).

[19] O. Kennedy, J. Burnett, J. Fenton, N. Constantino, P. Warburton, J. Morton, and E. Dupont-Ferrier, Tunable Nb Superconducting Resonator Based on a Constriction Nano-SQUID Fabricated with a Ne Focused Ion Beam, Phys. Rev. Appl. **11**, 014006 (2019).

[20] I. C. Rodrigues, D. Bothner, and G. A. Steele, Coupling microwave photons to a mechanical resonator using quantum interference, Nat. Commun. **10**, 5359 (2019).

[21] D. Bothner, I. C. Rodrigues, and G. A. Steele, Photon-Pressure Strong-Coupling between two Superconducting Circuits, arXiv:1911.01262 (2019).

[22] See Supplemental Material at http://link.aps.org/supplemental/10.1103/PhysRevApplied.14.024069 for details of device fabrication, device parameters, hysteresis of switching currents, measurement setup, data processing, and mathematical derivations.

[23] M. Tinkham, *Introduction to Superconductivity* (McGraw-Hill, Inc., New York, 1996), 2nd ed.

[24] W. J. Skocpol, M. R. Beasley, and M. Tinkham, Self-heating hotspots in superconducting thin-film microbridges, J. Appl. Phys. **45**, 4054 (1974).

[25] D. Hazra, L. M. A. Pascal, H. Courtois, and A. K. Gupta, Hysteresis in superconducting short weak links and μ-SQUIDs, Phys. Rev. B **82**, 184530 (2010).

[26] N. Kumar, T. Fournier, H. Courtois, C. B. Winkelmann, and A. K. Gupta, Reversibility Of Superconducting Nb Weak Links Driven By The Proximity Effect In A Quantum Interference Device, Phys. Rev. Lett. **114**, 157003 (2015).

[27] S. Pogorzalek, K. G. Fedorov, L. Zhong, J. Goetz, F. Wulschner, M. Fischer, P. Eder, E. Xie, K. Inomata, T. Yamamoto, Y. Nakamura, A. Marx, F. Deppe, and R. Gross, Hysteretic Flux Response and Nondegenerate Gain of Flux-Driven Josephson Parametric Amplifiers, Phys. Rev. Appl. **8**, 024012 (2017).

[28] R. L. Kautz and J. M. Martinis, Noise-affected I-V curves in small hysteretic Josephson junctions, Phys. Rev. B **42**, 9903 (1990).

[29] A. J. Annunziata, D. F. Santavicca, L. Frunzio, G. Catelani, M. J. Rooks, A. Frydman, and D. E. Prober, Tunable superconducting nanoinductors, Nanotechnology **21**, 445202 (2010).

[30] M. R. Vissers, J. Hubmayr, M. Sandberg, S. Chaudhuri, C. Bockstiegel, and J. Gao, Frequency-tunable superconducting resonators via nonlinear kinetic inductance, Appl. Phys. Lett. **107**, 062601 (2015).

[31] J. Gao, J. Zmuidzinas, B. A. Mazin, P. K. Day, and H. G. Leduc, Experimental study of the kinetic inductance fraction of superconducting coplanar waveguide, Nucl. Instrum. Methods Phys. Res. Sec. A **559**, 585 (2006).

[32] C. Eichler and A. Wallraff, Controlling the dynamic range of a Josephson parametric amplifier, EPJ Quantum Technol. **1**, 2 (2014).

[33] C. Rauscher, V. Janssen, and R. Minihold, *Fundamentals of Spectrum Analysis* (Rohde & Schwarz, München, 2016), 9th ed., oCLC: 964521293.

[34] L. Planat, R. Dassonneville, J. P. Martínez, F. Foroughi, O. Buisson, W. Hasch-Guichard, C. Naud, R. Vijay, K. Murch, and N. Roch, Understanding the Saturation Power of Josephson Parametric Amplifiers Made from SQUID Arrays, Phys. Rev. Appl. **11**, 034014 (2019).

[35] M. F. Gely, G. Steele, 'QuCAT, Quantum circuit analyzer tool in python, New J. Phys.**22**, 013025 (2019).

[36] S. Noschese, L. Pasquini, and L. Reichel, Tridiagonal Toeplitz matrices: Properties and novel applications, Numerical Linear Algebra Appl. **20**, 302 (2013).

[37] S. E. Nigg, H. Paik, B. Vlastakis, G. Kirchmair, S. Shankar, L. Frunzio, M. H. Devoret, R. J. Schoelkopf, and S. M. Girvin, Black-Box Superconducting Circuit Quantization, Phys. Rev. Lett. **108**, 240502 (2012).

[38] U. Vool and M. Devoret, Introduction to quantum electromagnetic circuits, Int. J. Circuit Theory Appl. **45**, 897 (2017).

[39] R. N. Simons, *Coplanar Waveguide Circuits, Components, and Systems*, edited by K. Chang, Wiley Series in Microwave and Optical Engineering (John Wiley & Sons, Inc., New York, USA, 2001).

[40] F. E. Schmidt, D. Bothner, I. C. Rodrigues, M. F. Gely, M. D. Jenkins, and G. A. Steele, Data and processing for "Current detection using a Josephson parametric upconverter" (2020).